This article has been accepted for publication in a future issue of this journal, but has not been fully edited. Content may change prior to final publication. Citation information: DOI 10.1109/TAP.2021.3066247, IEEE Transactions on Antennas and Propagation

Postprint of: Ullah U., Al-Hasan M., Mabrouk I., Kozieł S., Series-Slot-Fed Circularly Polarized Multiple-Input-Multiple-Output Antenna Array Enabling Circular Polarization Diversity for 5G 28-GHz Indoor Applications, IEEE TRANSACTIONS ON ANTENNAS AND PROPAGATION, (2021), pp. 1-9, DOI: 10.1109/TAP.2021.3066247

Series-Slot-Fed Circularly Polarized Multiple-Input-Multiple-Output Antenna Array Enabling Circular Polarization Diversity for 5G 28-GHz Indoor Applications

Ubaid Ullah, *Member IEEE,* Muath Al-Hasan, *Senior Member, IEEE,* Slawomir Koziel, *Senior Member, IEEE,* and Ismail Ben Mabrouk, *Senior Member, IEEE*

***Abstract*—In this paper, a four-element circularly polarized series-slot-fed multiple-input-multiple-output (MIMO) antenna array with circular polarization diversity is presented. The proposed design utilizes a combination of 45-degree inclined slots and a straight microstrip line feeding technique. The two antennas are designed to operate with the opposite sense of circular polarization (CP). CP is achieved by placing a patch of just about square dimensions on the top of the V-slot with orthogonal but unequal arms. The unequal arm of the slot degenerates the fundamental mode at a slightly different frequency with 90-degree phase difference occurring at the center frequency of each arm. Proper positioning of the patch on the top of the slot ensures excitation of CP. For realizing a MIMO antenna with different sense of polarization, both the slots and the patches are flipped with respect to the feedline. Following optimization at the full-wave level of description, the antenna is prototyped and validated experimentally. The realizable antenna footprint is 20 mm × 27.7 mm. The simulated and measured results indicate that the proposed antenna features a wide impedance bandwidth ($|S_{11}|$<-10 dB) from 26.9 GHz to 30.7 GHz, 3 dB axial ratio bandwidth from 27.31 GHz to 29.65 GHz and the peak realized gain of 11.86 dBic. Moreover, it exhibits a low level of in-band isolation $|S_{21}|$>-37 dB and almost negligible envelope correlation coefficient (ECC), less than 0.00025. The highly directional beams, high gain and compact size of the proposed antenna permit implementation of multiple antennas for indoor applications in the 28-GHz band.**

***Index Terms*— Multiple-input-multiple-output Antenna, Circular Polarization, Polarization Diversity, 5G, Series Array**

I. Introduction

In the recent years, the ever-increasing bandwidth requirements and improved channel capacity has encouraged the use of numerous unlicensed bands in the millimeter wave (mm-wave) range. Following the formal induction of the mm-wave band into the fifth generation (5G) technology, an exponential growth has been seen in the infrastructure development for the commercial use of 5G. The 28 GHz mm-wave band in particular has since gained significant attention due to its ability to cater enormous data rates, improved reliability and low power consumption [1-2]. The primary concern and the major shortcoming of the mm-wave band is the signal attenuation, high path losses, limited scattering, and absorption losses due to atmospheric changes. The combination of linearly polarized antennas and the inherent characteristic losses of the mm-wave band will have detrimental effects on the wireless communication, including intermittent connection, data loss, and faded signal [3-5]. Contrary to the linearly polarized antennas, the signal integrity can be enhanced by using circular polarization which alleviates polarization mismatches and multipath losses [6-8].

The use of single-element antenna further deters the already limited effective communication distances of wireless communication due to their low gain and scattered beams [9-10]. The size reduction of the circuit components at the high frequencies allows for flexible design strategy, in particular, developing antennas that can fit into the limited allocated space of modern compact devices. Accordingly, high performance arrays with directional beams have been considered to fully utilize the potential of the mm-wave band. A number of advanced antenna arrays with different types of feeding and radiator configuration have been proposed [11-17]. A variety of challenges are associated with the design of antenna arrays, and their implementation for mm-wave subsystems. For instance, in the parallel-fed array, the excitation of surface waves caused by the feedline discontinuities leads to unwanted radiation resulting in the degradation of the radiation efficiency [18]. Moreover, the complexity of the circuit and the auxiliary active components add to the production and power consumption cost thus hindering its commercial use. On the other hand, the series-fed antenna array offers a straightforward solution by utilizing single-port-fed short transmission lines. Owing to the simple architecture of the series-fed array, simultaneous implementation of multiple antenna design is fairly easy compared to parallel-fed arrays [19-21].

To meet the stringent performance requirements of the wireless communication at the mm-wave band, a deployment of multiple-input-multiple-output (MIMO) technology, as well as the development of highly directional antennas is an essential prerequisite. MIMO technology has long proven its potential in improving the channel capacity of the wireless communication system and has been actively investigated for mm-wave applications [22-27]. The spatial correlation between the MIMO antenna is an important design consideration in determining the system performance. In [28], a detailed study has been carried out

This article has been accepted for publication in a future issue of this journal, but has not been fully edited. Content may change prior to final publication. Citation information: DOI 10.1109/TAP.2021.3066247, IEEE Transactions on Antennas and Propagation

on the performance analysis of MIMO antenna with different array factor and polarization configurations in the mm-wave band. It has been established that MIMO antennas operating with dual polarization or circular polarization has a better channel capacity than the alternatives. As of now, there has been some research done on linearly polarized orthogonally placed MIMO antennas for mm-wave band, which has shown a promising performance [29-31]. But to date, a very limited amount of work has been done on CP MIMO antenna array with polarization diversity for the mm-wave band.

Following the above discussion and to address the design challenges in the mm-wave band, a cost-efficient and easy-to-fabricate circularly polarized MIMO antenna with polarization diversity is presented. The proposed antenna is comprised of two parallel-placed microstrip line fed series aperture coupled 45-degree inclined patches. Circular polarization in the nearly square patch (with the aspect ratio of more than 1.1) is induced by the orthogonal arms of the inclined slots. The unequal arms of the slot split the fundamental resonant mode of the patch into near degenerate mode at a slightly different frequency with the 90-degree phase difference occurring the center frequency of each mode. To realize the polarization diversity, the sense of current rotation is altered by simply flipping the slots and patches with respect to the feedline. By adopting this approach to design the CP MIMO antenna, a negligible level of envelop correlation coefficient (ECC) is obtained due to the inverse correlation in the radiated far-fields. The simulated and measured results demonstrate that the antenna retains wide impedance bandwidth from 26.9 GHz to 30.7 GHz and 3 dB axial ratio (AR) bandwidth from 27.31 GHz to 29.65 GHz. Moreover, the peak realized gain of the antenna is 11.86 dBic, which is attributed to the highly directional beams in the broadside direction. To further prove the potential of the proposed antenna for indoor application, four antennas can be placed in the ring or six in the hexagon configuration to enhance the coverage. The polarization diversity, low level of back-lobe, low complexity and good integration ability of the proposed antenna allows for implementation of the uniformly spaced ring architecture providing 360-degreee coverage.

II. Antenna Design and MIMO Configuration

The geometrical configuration of the proposed multi-layer MIMO antenna and the parameterized view is shown in Fig. 1. The proposed series array antenna utilizes a simple aperture coupling technique to realize the two-port MIMO design. All the four layers of the antenna are printed on Rogers RO4003C substrate (epsilon= 3.38, thickness = 0.508 and loss tangent= 0.0027) with the external dimensions of $w_s \times l_s$. The individual layers are shown in Fig. 1(a) and the stacking order is shown in Fig. 1(b). The total thickness of the antenna is roughly 2.5 mm. Layer 1 is a plane metallic layer placed a quarter wavelength away from the radiator to ensure constructive correlation of the reflected wave with the radiating wave in the broadside direction. Two straight microstrip lines with the matching stubs at the open end are printed parallel to each other on one side of the substrate labeled as Layer 2. Furthermore, V-shaped slots with orthogonal arms were etched on the back side of the ground plane, indicated as Layer 3. The 45-degree inclined slots are designed to have uneven arm dimensions, and spaced half guided wavelength from each other in the *y*-direction. The aperture-coupled identical radiating patch elements are printed on Layer 4 and stacked on the top of the slot. The dimensions of the slot and the patch are shown in the enlarged section of the Figure. To achieve proper coupling, the slots are inclined with respect to the microstrip line and the radiating patches are adjusted on the top of the slots. To implement the MIMO design, the position of the slots and the radiating patches are switched from the left-hand-side of the microstrip line to its right-hand-side. This simple geometrical alteration leads to the excitation of different sense of circular polarization in the MIMO antenna.

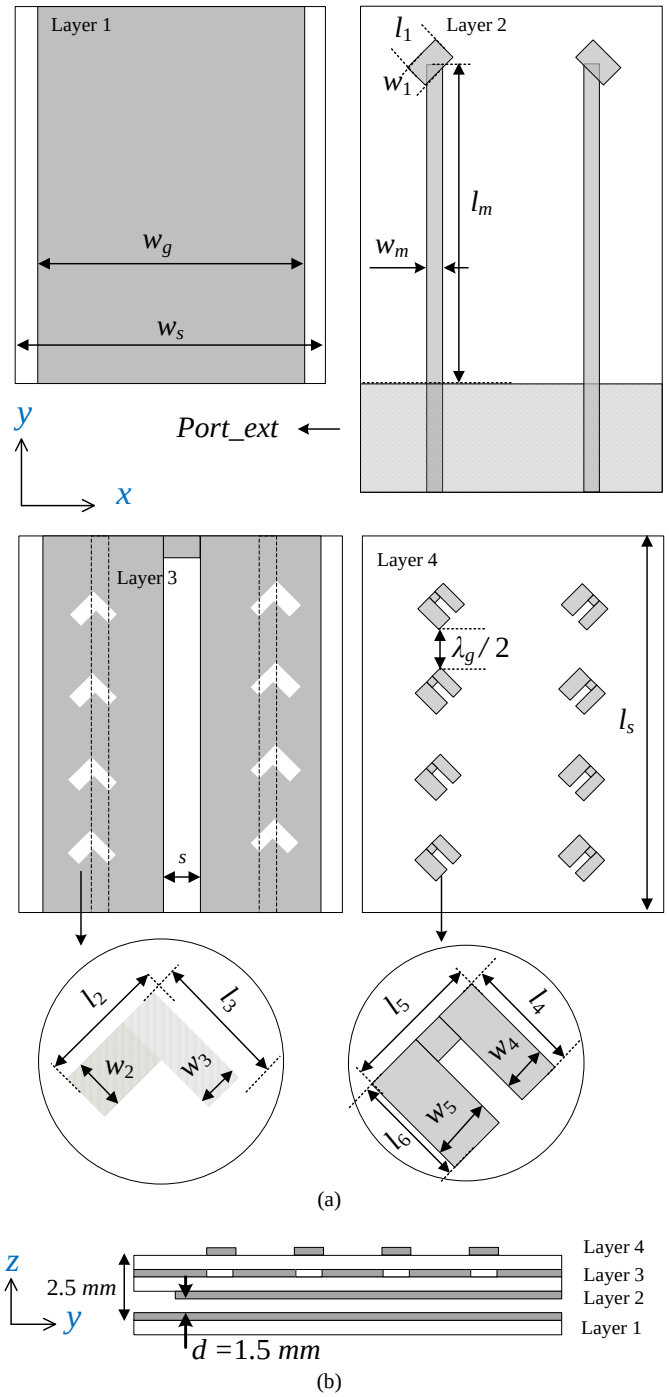

Fig. 1. Geometry of the proposed CP MIMO antenna with polarization diversity.

III. Theoretical Analysis And Circular Polarization Mechanism

A. Theoretical background and analysis

It is important to understand the theoretical background of the aperture coupled microstrip patch antenna for design implementation of a wideband CP antenna at the mm-wave band. The position of the patch radiator with respect to the magnetic current source, the dimensions of the patch, and the orientation angle of the slot with respect to the feedline are the key factors. For initiating the design process, the nearly square shape patch dimensions are calculated to operate at 28 GHz. The patch geometry shown in Fig. 2 with $a > b$ allows for excitation of near degenerate mode, while the resonant wavenumber k of the modes is of the order $k_{01} = \pi/b$ and $k_{01} = \pi/a$. As the wavenumbers are close to each other, it is assumed that the quality (Q) factor value will be the same for both of the frequencies. The effective wavenumber including the losses for both the modes can be written as:

$$k \cong k_0\sqrt{\varepsilon_r}\left(1 - j\frac{1}{2}Q\right) \tag{1}$$

When the condition $Q >> 1$ is satisfied for both the radiating modes, the excitation frequencies for the said dimensions of the patch satisfy the condition $f_{10} < f < f_{01}$. The field radiated by the antenna along the z-direction will have the form

$$E = \hat{x}E_x + \hat{y}E_y \tag{2}$$

For an arbitrary orientation of the slot with respect to the feedline, the electric field in the x- and y-direction are expressed as:

$$E_x \propto \frac{sin\left(\pi w\frac{sin\theta}{2a}\right)sinc\left(\pi l\frac{cos\theta}{2a}\right)\sin(\pi x_0/a)}{k-k_{10}} \tag{3}$$

$$E_y \propto -\frac{sin\left(\pi w\frac{sin\theta}{2b}\right)sinc\left(\pi l\frac{cos\theta}{2b}\right)\sin(\pi y_0/b)}{k-k_{01}} \tag{4}$$

where, l and w, are the length and the width of the slot, respectively, whereas θ is the angle of orientation of the slot.

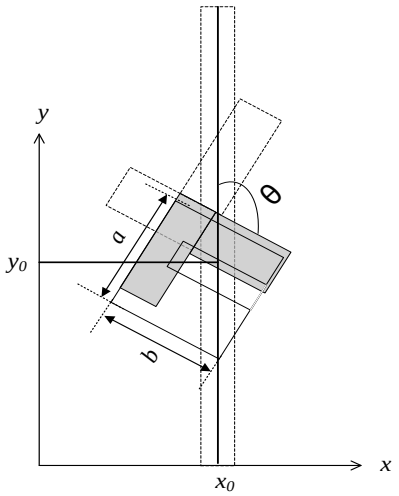

Fig. 2. Configuration of the inclined slot-fed patch.

As for circular polarization, excitation of two orthogonal components with equal amplitude is a precondition, therefore, by using equation (3) and (4)

$$\frac{E_y}{E_x} \cong A\frac{k-k_{10}}{k-k_{01}} = \pm J \tag{5}$$

The plus and the minus sign indicate the sense of circular polarization as right-hand CP and left-hand CP, respectively. The coefficient A in (5) is calculated as

$$A = \frac{sin\left(\pi w\frac{sin\theta}{2b}\right)sinc\left(\pi l\frac{cos\theta}{2b}\right)\sin(\pi y_0/b)}{sin\left(\pi w\frac{sin\theta}{2a}\right)sinc\left(\pi l\frac{cos\theta}{2a}\right)\sin(\pi x_0/a)} \tag{6}$$

For effective excitation of CP, the feed position (x_0, y_0) is an important factor and can be determined by:

$$\mathrm{A} = \pm\,|\mathrm{A}| \tag{7}$$

Where, A on the left side is given by (6). |A| can be found using the relation [32]

$$|A| = \frac{a-b}{b}\,Q \pm \sqrt{\left(\frac{a-b}{b}Q\right)^2 - \frac{a}{b}} \tag{8}$$

As for the slot coupled radiator, most of the energy is confined in the slot-center. Consequently, in this work, the V-shape slot is curved with the 90-degree bend in the center. The unequal arm dimensions ensure the excitation of slightly different frequencies satisfying $f_{10} < f < f_{01}$. Referring to (3) and (4), it can be observed that the strength of the two modal fields is determined by the length, the width and the orientation angle of the slot. The slot position and the orientation angle θ is an important consideration for the excitation of antenna radiating fields as it controls the level of coupling to the patch radiators. For instance, with the horizontal orientation of the slot (θ = 0°) with respect to the feedline, the TM_{10} cannot be excited with a horizontally oriented field component. Moreover, the vertically oriented field components for the angle (θ = 90°), TM_{01} will not be excited.

Simultaneous excitation of both modes requires the coupling fields to be oriented in both the x- and y-direction. Therefore, the V-shape slot is inclined by 45-degrees. For initiating the design process, the nearly square shape patch dimensions are approximated to operate at 28 GHz. The radiating patches are stacked on the top of the slot so that each radiating edge is aligned with the orthogonal arms of the slot. The off-center slit in the patch creates additional current path along the shorter edge and improves the impedance bandwidth. The longer arm of the slot excites the radiating mode at the lower frequency (f_{10}), whereas the shorter arm excites the high frequency mode (f_{01}). The 90-degree phase difference occurs at the center frequency of each arm resulting in circular polarization. For altering the sense of polarization, the position of the slots is switched with respect to the microstrip line. To clearly show the rotation of the current for each sense of polarization, the equivalent field are sketched and illustrated in Fig. 3.

When the slot and the patches are inclined to the left-hand-side of the feedline as shown in Fig. 2, right-hand CP (RHCP) is excited, and left-hand CP (LHCP) for inclination towards right.

This article has been accepted for publication in a future issue of this journal, but has not been fully edited. Content may change prior to final publication. Citation information: DOI 10.1109/TAP.2021.3066247, IEEE Transactions on Antennas and Propagation

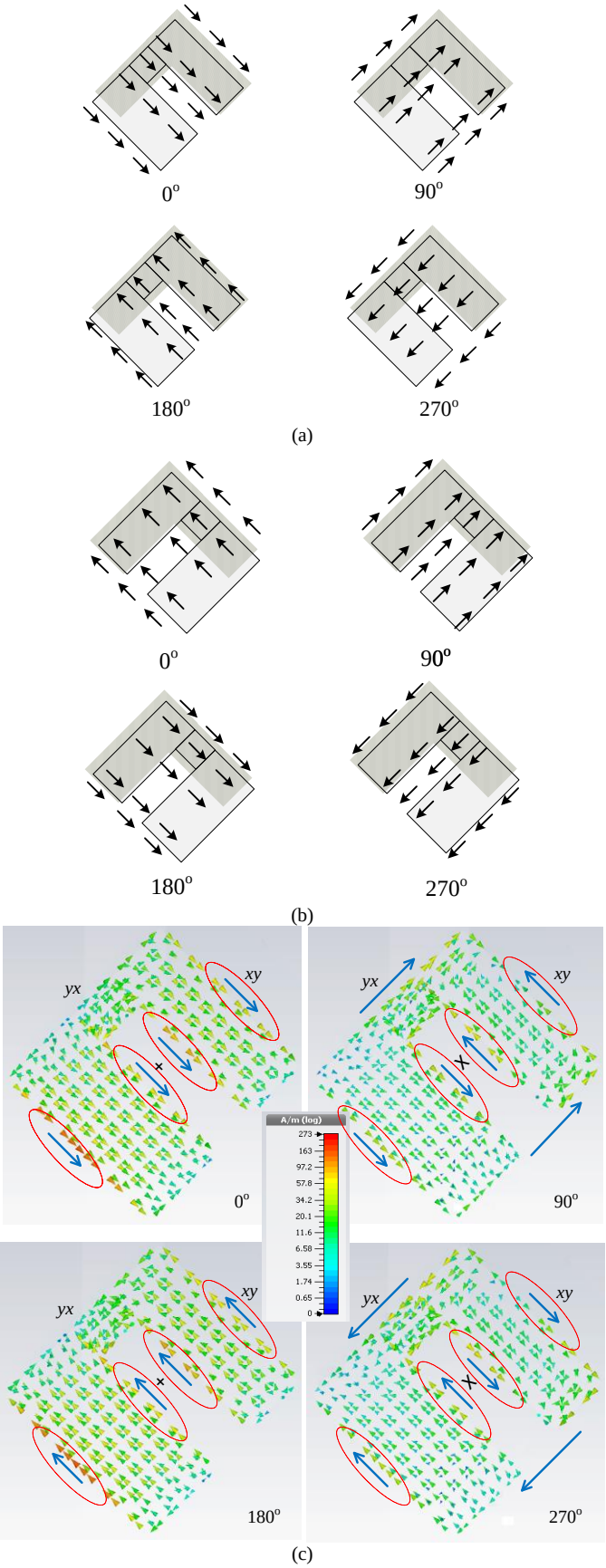

Fig. 3. Sketch of the dominant field component at different time intervals: (a) RHCP, (b) LHCP, (c) Simulated RHCP.

To further clarify the operation mechanism of the antenna, the simulated field for RHCP distribution is shown in Fig. 3(c). At zero degrees, the dominant field components are oriented along the *xy*-direction and the fields on the edges adds up in phase. At 90 degrees, the dominant field orientation changes to the *yx*-direction due to the field cancelation along the *xy*-direction. Similarly, at 180 degrees, and 270 degrees, the dominant field orientation changes to *–xy*- and *–yx*-direction respectively. A small difference in the magnitude of the dominant fields *yx*- and *xy*-direction can be observed, which is due to the slight asymmetrical position of the slot arms with respect to the feedline. The magnitude can be adjusted by a precise positioning of the slots.

As it can be seen, the field traces a counterclockwise path with the phase progression; therefore, the sense of polarization is RHCP. For the implementation of the series inclined-slot-fed array the four elements are spaced half guided-wavelength ($\lambda_g/2$ = 2.914 mm) from each other. This configuration ensures equal coupling of all the radiators with uniform phase and circumvent existence of pattern null in the broadside direction. Following the initial modeling based on the theory, the antenna is optimized at the full-wave level of description.

B. Antenna Optimization

In engineering practice, inefficient optimization procedures such as parameter sweeping are still widely used. Notwithstanding, to account for high sensitivity of the mm-wave band, high-cost of EM simulation, handling of large set of parameters and simultaneous optimization of several performance figures, demands for development of more effient and reliable optimization techniques. In this work, a multi-stage full-wave optimization process is use to fully optimize the proposed antenna. To describe the optimization process, the impedance bandwidth of the antenna is indicated as $BW_S(\boldsymbol{x})$ (i.e., the frequency range for which $|S_{11}| \leq -10$ dB), whereas $S(\boldsymbol{x})$ will show the maximum in-band reflection level. Also, the symbol $AR(\boldsymbol{x})$ is used to denote the maximum in-band value of axial ratio (AR). The vector of adjustable antenna parameters is denoted as $\boldsymbol{x}$.

The design specifications are as follows:

- Maximize $BW_S(\boldsymbol{x})$ around 28 GHz;
- Minimize $AR(\boldsymbol{x})$ within the pre-optimized impedance bandwidth;
- Ensure that $S(\boldsymbol{x}) \leq -10$ dB for the entire *AR* bandwidth;

At the first stage, the highly sensitive parameters with respect to both the performance figures, i.e., $|S_{11}|$ and *AR* were identified using sensitivity analysis. Following the optimization of these parameters, the full set of variable are optimized by solving the minimization task formulated as

$$\boldsymbol{x}^* = \arg\min_{\boldsymbol{x}} U\left(BW_S(\boldsymbol{x}), S(\boldsymbol{x}), AR(\boldsymbol{x})\right) \tag{9}$$

where *U* is the objective function. Moreover, two separate sub-problems were considered. Firstly, the objective function for the optimization of impedance bandwidth is defined as:

$$U_S\left(BW_S(\boldsymbol{x}), S(\boldsymbol{x}), AR(\boldsymbol{x})\right) = -BW_S(\boldsymbol{x}) \tag{10}$$

For the optimization of *AR*, the objective function is defined as:

$$U_{AR}\left(BW_S(\boldsymbol{x}), S(\boldsymbol{x}), AR(\boldsymbol{x})\right) = AR(\boldsymbol{x}) + \beta_S c_S\left(S(\boldsymbol{x})\right)^2 \tag{11}$$

where, $c_S(S(\boldsymbol{x})) = \max\{(S(\boldsymbol{x}) + 10,0\}/10$ is a penalty function and β_S is a penalty factor. The purpose of imposing the penalty function is to measure a relative violation of the condition $S(\boldsymbol{x}) \leq -10$ dB.

Solving (9) with the objective function (10) ensures maximizing the antenna impedance bandwidth with adequate in-band impedance matching. Whereas, the goal of solving (9) with the objective function (11) is to minimize *AR*, below 3 dB reference for as much of the previously obtained impedance bandwidth as possible. Both sub-problems are solved by means of the trust-region (TR) gradient search with the antenna response gradients estimated using finite differentiation [33]. The TR procedure produces a series $\boldsymbol{x}^{(i)}$, $i = 0, 1, \ldots$, of approximations to $\boldsymbol{x}^*$, where the new point $\boldsymbol{x}^{(i+1)}$ is obtained by solving the following sub-problem

$$\boldsymbol{x}^{(i+1)} = \arg\min_{\|\boldsymbol{x}-\boldsymbol{x}^{(i)}\| \leq d^{(i)}} L^{(i)}(\boldsymbol{x}) \tag{12}$$

where $L^{(i)}$ is an objective function computed using linear (first-order Taylor) expansion models of the antenna characteristics. As mentioned before, the antenna response sensitivity are obtained by means of finite differentiation. The problem (12) is solved in the vicinity of the current iteration point $\boldsymbol{x}^{(i)}$ with the trust region size adaptively adjusted using the standard TR rules (cf. [33]).

The step-by-step optimization of impedance bandwidth followed by the AR bandwidth allows for effective handling of all performance figures. The final optimized parameters values (in millimeter) are listed in Table I. The CPU cost of the optimization process is 237 EM simulations of the antenna (~154 hours) for the first stage, and 178 EM analyses (~115 hours) for the second stage. The overall expenses amount to around 269 hours of the CPU time. Although these numbers may seem high in terms of the CPU (but not the number of EM analyses), the reason is that antenna simulation takes about 40 minutes, which is both due to a highly-graded meshes and the incorporation of the connector into the computational model. At the same time, it should be noted that the cost of a single iteration of the TR algorithm is proportional to the number n of antenna parameters, and the overall complexity is better than n^2 for practical antenna problems. Thus, the overall number of EM analyses (415) is relatively low given that the structure is described by seventeen independent parameters. Notwithstanding, the optimization process is automated at each stage of the process.

C. Parametric Analysis

A detailed parametric study is performed to evaluate the performance of the antenna in terms of impedance matching and AR. The parameters defining the dimensions of the patch and the slot are of high importance in attaining the desired performance. The relationship between the simulated impedance matching and AR for the length l_2 indicates that by reducing the length from the optimized value, the AR shifts upward, while the impedance matching shows a slight degradation and a downward shift. The length l_3 of the slot exhibits a similar type of effect. When the length is altered from the optimized value, an upward shift in the resonance as well as the AR is observed.

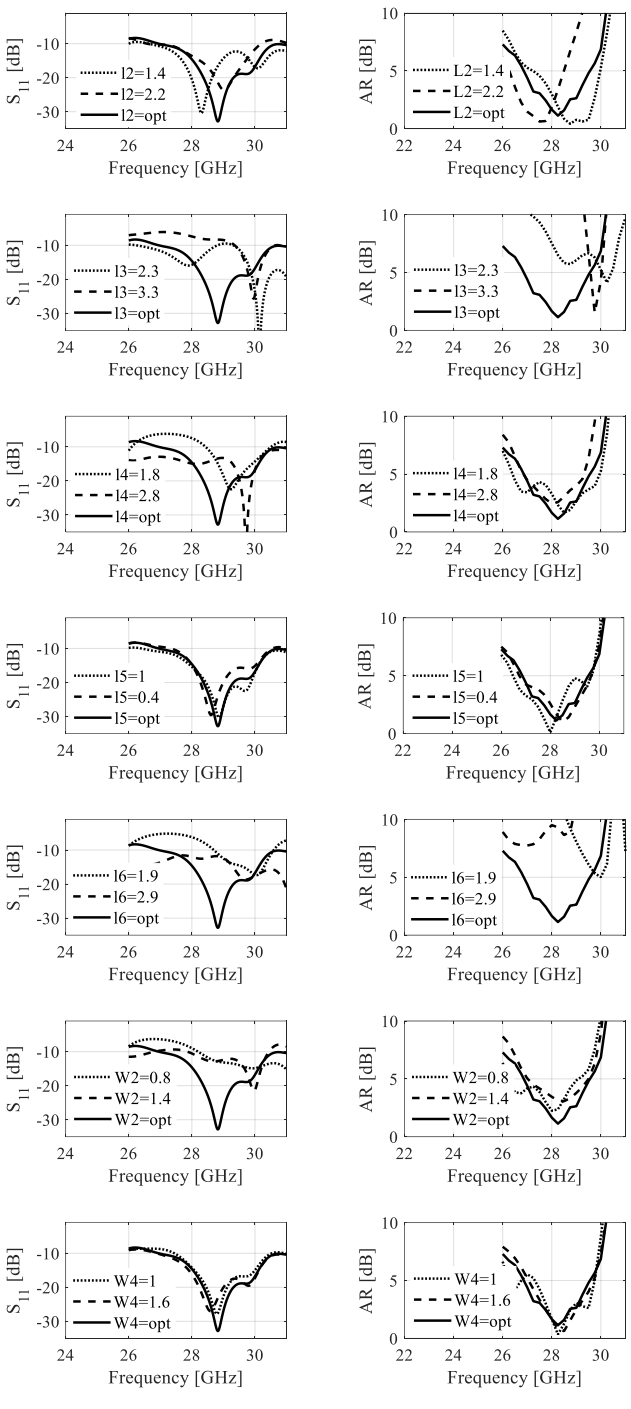

Fig. 4. Parametric analysis of the antenna in terms of (a) impedance matching and, (b) AR.

TABLE I Optimized Parameter Values

Parameter	Value	Parameter	Value	Parameter	Value
l_1	2.7	l_4	2.37	l_s	28.7
w_1	1.81	w_4	0.862	w_s	27
l_2	3.12	l_5	2.767	w_g	24
w_2	1.1	w_m	1.05	l_m	27.14+5.828
l_3	2.85	w_3	1.327	l_6	2.427
s	4	w_{g1}	10		

Decreasing the length of the patch l_4 leads to the resonance shifting upward; when it is increased, the frequency shifts downward. A small degradation in the AR is also observed with the reduction of the patch length. Changing the length l_5 marginally affects the performance of the antenna both in terms of S_{11} and AR. On the other hand, the length l_6 of the U-shape slot is of importance. When it is decreased with respect to the optimum value, the operating frequency shifts upward, and both the impedance matching and AR are considerably degraded. Similarly, the increase of l_6 results in shifting the operating frequency downwards, but also poor impedance matching. Parameter W_2 mainly controls the operating frequency of the antenna and the impedance matching, whereas AR is marginally affected. Finally, the effects of altering the parameter W_4 are shown, which illustrate negligible change in both the impedance matching and AR. It should be noted that these parameters are analyzed individually; their mutual dependence is not accounted for.

IV. Experimental Validation and Discussion

The proposed CP MIMO antenna with polarization divesity has been fabricated using the printed circuit board (PCB) technology and charecterized experimentaly in the anechoic chamber of Reykjavik University, Iceland. The Southwest end-launch connectors (1092-03A-6) are mounted on the excitation layer. To accommodate the connectors, the length and the width of the Layer 2 is extended. For maintaining the injection of excact phases to each radiator in the series array, the length of the feed layer is extended along the –*y*-direction. To ensure proper mechnical alignment of all the layers, only the widths of other layers are extended ±*x*-direction. In practice, the antenna can be realized with the external dimesion $w_g \times l_s$ = 24 mm × 28.7 mm. All the layers are stacked in the order shown in Fig. 1(b). The front view, back view and the perpective view of the final prototype is shown in Fig. 5. All the major performance figures of the antenna are charecterized for both ports.

A. S-parameters and Axial Ratio

The simulated and measured reflection coefficient of the proposed antenna is shown in Fig. 6. The results demonstrate that the antenna covers a wide impedance bandwidth from 26.9 GHz to 30.7 GHz. The isolation (S_{21}) of the antenna is shown in Fig. 7. Both the simulated and measured result shows that the proposed antenna exhibits excellent port-to-port isolation (< -37 dB) in the entire operating band. The reason for improved isolation is the inherent property of polarization diversity and the added spacing for port mounting.

The simulated and the measured axial ratio of the antenna is shown in Fig. 8. The 3 dB axial ratio results demonstrate that the CP bandwidth of the antenna is from 27.31 GHz to 29.65 GHz.

B. Envelop Correlation Coefficient and Diversity Gain

The ECC is one of the crucial consideration that describes the MIMO antenna performance in terms of correlation between the two closely-spaced antennas. Since the channel capacity of a wireless system directly depends on this parameter, the lower the correlation the better the signal integrity and the channel capacity. As the far-field correlation between the two antennas greatly affects the performance of the antenna, the ECC of the proposed antenna is therefore calculated using the following field-based formula

$$ECC = \rho e = \frac{\left|\iint_{4\pi}\left[\overrightarrow{F_i}(\theta,\phi)*\overrightarrow{F_j}(\theta,\phi)\right]d\Omega\right|^2}{\iint_{4\pi}|\overrightarrow{F_i}(\theta,\phi)|^2*\iint_{4\pi}\overrightarrow{F_j}(\theta,\phi)|^2} \quad (13)$$

$$DG = 10\sqrt{1-|\rho e|^2} \quad (14)$$

The calculated ECC of the proposed antenna is shown in Fig. 9. It can be observed from the level of correlation that the fields radiated by the antenna with circular polarization diversity are almost entirely uncorrelated. The recorded ECC < 0.00025 shows that the antenna has a very low level of correlation, which can be ascribed to the implementation of CP diversity. Furthermore, the diversity gain (DG) of the antenna is calculated using (14). Since DG is directly dependent on the ECC, the plot of the calculated DG shown in Fig. 10 confirms that maximum diversity gain is achieved.

C. Realized Gain and Radiation Pattern

Figure 11 illustrates the simulated and measured realized gain of the antenna. The peak gain of the antenna is recorded to be approximately 11.86 dBiC near the frequency of 28 GHz. A relatively stable gain in the operating band of the antenna is observed with in-band variation of roughly 1 dB. Finally, the far-field patterns of the antenna are shown for both the ports in the *xz*- and *yz*-planes. To verify that the proposed antenna retains highly directional beams in the operating band, the radiation patterns are characterized at four frequency points, i.e., 27.5 GHz, 28 GHz, 28.5 GHz and 29 GHz, but for the sake of brevity, only two frequency points are shown. The normalized far-field patterns are shown in Fig. 12 and Fig. 13 for Port 1 and Port 2, respectively.

The patterns in both the *xz*- and *yz*-planes exhibit stable radiation in the broadside direction with the low level of cross-polarized fields and the side lobes. The cross-polarization level is 20 dB lower than the co-polarized fields in the direction of maximum radiation. For Port 1, the co-polarized fields are right-hand CP, whereas for Port 2, it is left-hand CP. It should be noted that, for the series-fed array, the antenna elements are positioned along the *y*-direction, therefore, the *yz*-plane is of utmost importance. From the figures, it can be seen that the proposed array yields highly directional beams which corresponds to the excellent combination of the field vectors of the antenna elements.

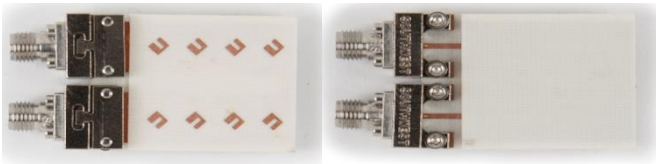

(a) (b)

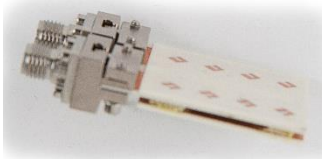

(c)

Fig. 5. Fabricated prototype of the proposed MIMO antenna: (a) top view, (b) back view, (c) perspective view.

This article has been accepted for publication in a future issue of this journal, but has not been fully edited. Content may change prior to final publication. Citation information: DOI 10.1109/TAP.2021.3066247, IEEE Transactions on Antennas and Propagation

TABLE II COMPARISON WITH THE RECENT STATE-OF-THE-ART MILLIMETER-WAVE ANTENNAS

Reference	Operating frequency (GHz)	Antenna type	Polarization	Size [λ_o^2]	Radiation Efficiency (%)	Peak Gain	%AR	%BW	Cost	Realization
[34]	28	Patch + DGS	Linear	0.27	80	8.3	----	14.6	High	Hard
[35]	30	Patch + Superstrate	Circular	0.35	---	8	6	19	High	Medium
[36]	28	Patch + Superstrate	Circular	0.7	---	14	17	27	High	Medium
[37]	28	Vivaldi Antenna	Circular	0.5	82	8	3	6	Low	Hard
[38]	24	Patch + EBG	Linear	----	80.5	6	---	3	High	Hard
[39]	28	Cross dipole	Circular	0.15		2.2	8	8	Low	Easy
Proposed	28	Patch	Circular	0.22	91	11.9	8.3	13.2	Low	Easy

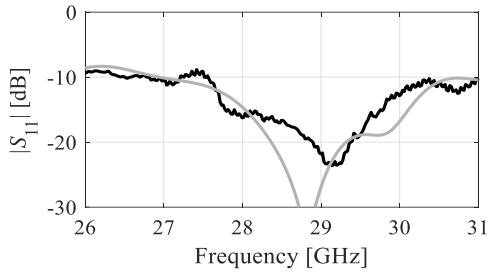

Fig. 6. Simulated (gray) and measured (black) impedance bandwidth.

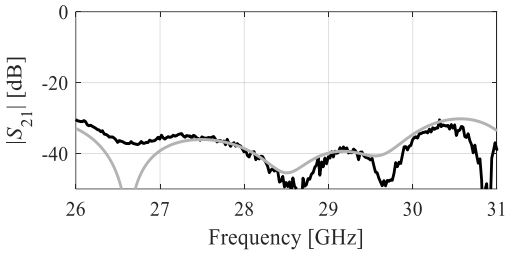

Fig. 7. Simulated (gray) and measured (black) isolation (S_{21}).

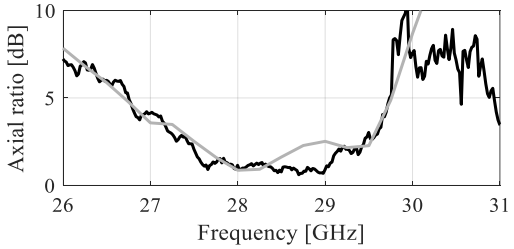

Fig. 8. Simulated (gray) and measured (black) axial ratio.

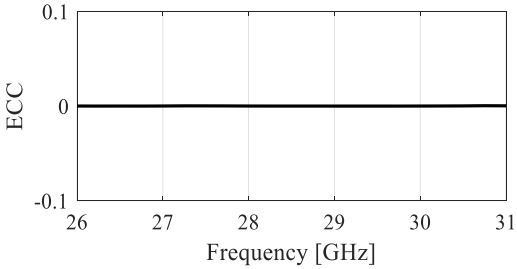

Fig. 9. Calculated envelop correlation coefficient of antenna.

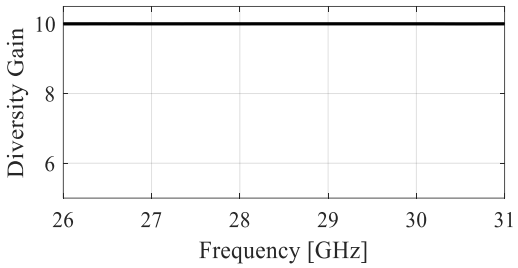

Fig. 10. Calculated diversity gain of antenna.

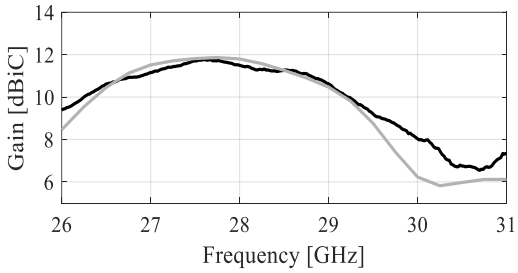

Fig. 11. Simulated (gray) and measured (black) realized gain.

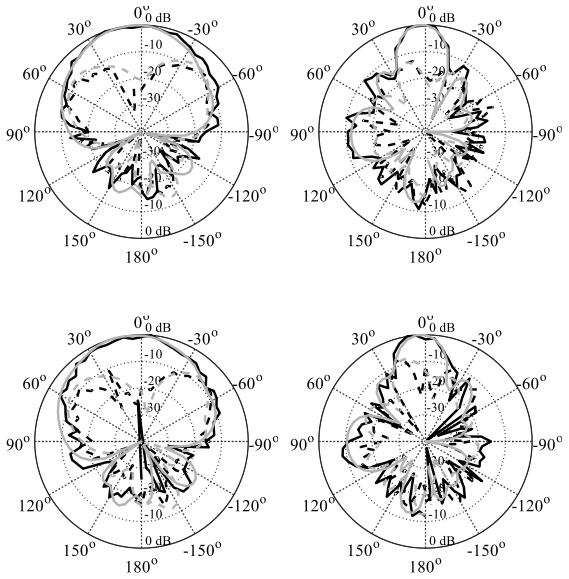

Fig. 12. Simulated (gray) and measured (black) *xz*- (left) and *yz*-plane (right) patterns for Port 1 at 28 GHz, and 29.0 GHz (from top to bottom); co-pol (—), cross-pol (- - -).

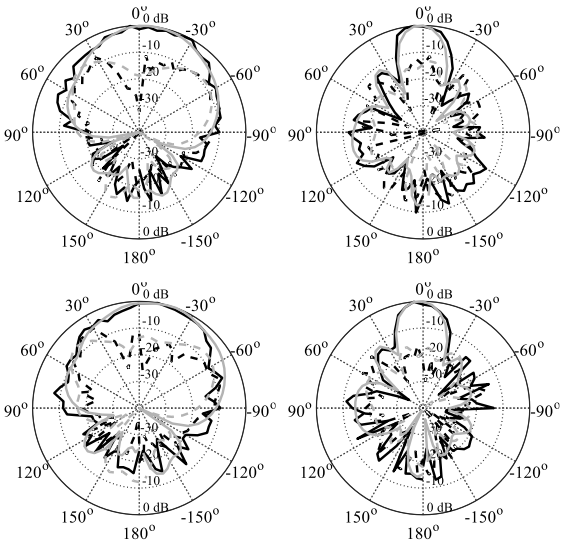

Fig. 13. Simulated (gray) and measured (black) *xz*- (left) and *yz*-plane (right) patterns for Port 2 at 28 GHz, and 29.0 GHz (from top to bottom); co-pol (—), cross-pol (- - -).

D. Benchmarking

The proposed antenna has been compared with the recent state-of-the-art millimeter-wave antennas in terms of multiple performance figures, cost, and implementation complexity. It should be noted that currently, there is a limited amount of work published on CP array for MIMO technology in the mm-wave range. Therefore, for fair comparison, the size reported in the table refers to that of a single element. From the comparison table, it can be observed that, the proposed antenna outperforms most of the recently published mm-wave designs. The performance of the antenna in ref [36] is better in terms of electrical characteristics, but the size, the complexity, and the cost of the circuit are reasonably high. Overall, the proposed antenna has better electrical characteristics, it is cost effective, and easy to realize.

V. CONCLUSION

In this paper, a dual circularly polarized series slot-fed MIMO antenna operating in the mm-wave 28 GHz band is presented. The proposed antenna is comprised of a straight microstrip-line-fed aperture coupled with radiating patch elements. Circular polarization is achieved by proper alignment of the patch element on the top of the 45-degree-inclined V-shape slots with orthogonal arms. By adjusting the nearly square patch on the top of the slot, the fundamental radiating mode is degenerated at slightly different frequency with the 90-degree phase difference occurring at the center frequency of each mode. Dual CP is achieved by simply switching the position of the slot and the patches with respect to the microstrip feedline. All of the adjustable parameters of the antenna are fully optimized before prototyping and characterization. Both the simulated and measured results confirm that the proposed MIMO antenna exhibits excellent performance in terms of major electrical and field properties. The advantages of the proposed antenna include highly directional beams, cost effectives, ease of fabrication, and realization of the prototype. Moreover, the directionality of the antenna permits implementation of multiple antenna in the ring arrangement for 360-degree coverage.

ACKNOWLEDGEMENT

The authors would like to thank Computer Simulation Technology AG, Darmstadt, Germany, for making CST Microwave Studio available.

REFERENCES

[1] C. Mao, S. Gao, and Y. Wang, "Broadband high-gain beam-scanning antenna array for millimeter-wave applications," *IEEE Trans. Antennas Propag*., vol. 65, no. 9, pp. 4864–4868, Sep. 2017.

[2] T. S. Rappaport et al., "Millimeter wave mobile communications for 5G cellular: It will work!" *IEEE Access*, vol. 1, pp. 335–349, May 2013.

[3] K. R. Mahmoud and A. M. Montaser, "Performance of tri-band multipolarized array antenna for 5G mobile base station adopting polarization and directivity control," *IEEE Access*, vol. 6, pp. 8682–8694, 2018.

[4] X. Wei, K. Zheng, and X. S. Shen, Eds. 5G Mobile Communications. Cham, Switzerland: Springer, 2017.

[5] O. M. Haraz, M. M. Ashraf, and S. Alshebili, "8×8 Patch antenna array with polarization and space diversity for future 5G cellular applications," *Proc. Int. Conf. IEEE Inf. Commun. Technol. Res. (ICTRC),* May 2015, pp. 258–261.

[6] U. Ullah, S. Koziel, and I. B. Mabrouk, "Rapid redesign and Bandwidth/Size tradeoffs for compact wideband circular polarization antennas using inverse surrogates and fast EM-based parameter tuning," *IEEE Trans. Antennas Propag.*, vol. 68, no. 1, pp. 81–89, Jan. 2020.

[7] U. Ullah, M. Al-Hasan, S. Koziel and I. B. Mabrouk, "Circular polarization diversity implementation for correlation reduction in wideband low-cost multiple-input-multiple-output antenna," *IEEE Access*, vol. 8, pp. 95585-95593, 2020.

[8] U. Ullah, I. B. Mabrouk, and S. Koziel, "A compact circularly polarized antenna with directional pattern for wearable off-body communications," *IEEE Antennas Wireless Propag. Lett.*, vol. 18, no. 12, pp. 2523–2527, Dec. 2019.

[9] J. Zhang, X. Ge, Q. Li, M. Guizani, and Y. Zhang, "5G millimeter-wave antenna array: Design and challenges," *IEEE Wireless Commun.*, vol. 24, no. 2, pp. 106–112, Apr. 2017.

[10] A. Ghosh, "The 5G mmWave radio revolution," *Microw. J.*, vol. 59, no. 9, pp. 3–10, 2016.

[11] K. R. Mahmoud and A. M. Montaser, "Design of dual-band circularly polarised array antenna package for 5G mobile terminals with beam-steering capabilities," *IET Microw., Antennas Propag*., vol. 12, no. 1, pp. 29–39, Jan. 2017.

[12] N. Ojaroudiparchin, M. Shen, S. Zhang et al., "A switchable 3-D-coverage-phased array antenna package for 5G mobile terminals," *IEEE Antennas Wirel. Propag. Lett.*, vol. 15, pp. 1747-1750, 2016.

[13] Y. Yang, B. Sun and J. Guo, "A single-layer wideband circularly polarized antenna for millimeter-wave applications," *IEEE Trans. Antennas Propag.*, vol. 68, no. 6, pp. 4925-4929, June 2020.

[14] J. Lan, Z. Yu, J. Zhou and W. Hong, "An aperture-sharing array for (3.5, 28) ghz terminals with steerable beam in millimeter-wave band," *IEEE Trans. Antennas Propag.*, vol. 68, no. 5, pp. 4114-4119, May 2020.

[15] H. Xu, J. Zhou, K. Zhou, Q. Wu, Z. Yu and W. Hong, "planar wideband circularly polarized cavity-backed stacked patch antenna array for millimeter-wave applications," *IEEE Trans. Antennas Propag.*, vol. 66, no. 10, pp. 5170-5179, Oct. 2018.

[16] Y. Li *et al*., "3-D printed high-gain wideband waveguide fed horn antenna arrays for millimeter-wave applications," *IEEE Trans. Antennas Propag*., vol. 67, no. 5, pp. 2868-2877, May 2019.

[17] K. Al-Amoodi, M. M. Honari, R. Mirzavand, J. Melzer, D. G. Elliott and P. Mousavi, "Circularly-polarised end-fire antenna and arrays for 5G millimetre-wave beam-steering systems," *IET Microw. Antennas Propag*., vol. 14, no. 9, pp. 980-987, 29 7 2020.

[18] M. Khalily, R. Tafazolli, T. A. Rahman and M. R. Kamarudin, "Design of phased arrays of series-fed patch antennas with reduced number of the controllers for 28-ghz mm-wave applications," *IEEE Antennas Wireless Propag. Lett.*, vol. 15, pp. 1305-1308, 2016.

[19] R. Chopra and G. Kumar, "Series-fed binomial microstrip arrays for extremely low sidelobe level," *IEEE Trans. Antennas Propag*., vol. 67, no. 6, pp. 4275-4279, June 2019.
[20] F. Kuo and R. Hwang, "High-isolation X-band marine radar antenna design," *IEEE Trans. Antennas Propag*., vol. 62, no. 5, pp. 2331-2337, May 2014.
[21] Y.-B. Jung, I. Yeom, and C. W. Jung, "Centre-fed series array antenna for k-/ka-band electromagnetic sensors," *IET Microw. Antennas Propag.*, vol. 6, no. 5, pp. 588–593, Apr. 2012.
[22] Y. Zhang, J. Deng, M. Li, D. Sun and L. Guo, "A MIMO dielectric resonator antenna with improved isolation for 5g mm-wave applications," *IEEE Antennas Wireless Propag. Lett.*, vol. 18, no. 4, pp. 747-751, April 2019.
[23] M. Ikram, N. Nguyen-Trong and A. Abbosh, "Multiband MIMO microwave and millimeter antenna system employing dual-function tapered slot structure," *IEEE Trans. Antennas Propag*., vol. 67, no. 8, pp. 5705-5710, Aug. 2019.
[24] K. R. Jha and S. K. Sharma, "Combination of MIMO antennas for handheld devices," *IEEE Antennas Propag. Mag.*, vol. 60, no. 1, pp. 118–131, Feb. 2018.
[25] D. Q. Liu, M. Zhang, H. J. Luo, H. L. Wen, and J. Wang, "Dual-band platform-free PIFA for 5G MIMO application of mobile devices," *IEEE Trans. Antennas Propag.*, vol. 66, no. 11, pp. 6328–6333, Nov. 2018.
[26] Q. Chen, H. Lin, J. Wang, L. Ge, Y. Li, T. Pei, and C.-Y.-D. Sim, "Single ring slot-based antennas for metal-rimmed 4G/5G smartphones," *IEEE Trans. Antennas Propag.*, vol. 67, no. 3, pp. 1476–1487, Mar. 2019.
[27] M. Aboualalaa *et al*., "Independent matching dual-band compact quarter-wave half-slot antenna for millimeter-wave applications," *IEEE Access*, vol. 7, pp. 130782-130790, 2019.
[28] S. Park, M. Jeong, K. Bae, D. Kim, L. Minz and S. Park, "Performance comparison of 2×2 mimo antenna arrays with different configurations and polarizations in reverberation chamber at millimeter-waveband," *IEEE Trans. Antennas Propag.*, vol. 65, no. 12, pp. 6669-6678, Dec. 2017.
[29] H. Huang, X. Li, and Y. Liu, "A low-profile, dual-polarized patch antenna for 5G MIMO application," *IEEE Trans. Antennas Propag*., vol. 67, no. 2, pp. 1275–1279, Feb. 2019.
[30] M.-Y. Li, Z.-Q. Xu, Y.-L. Ban, C.-Y.-D. Sim, and Z.-F. Yu, "Eightport orthogonally dual-polarised MIMO antennas using loop structures for 5G smartphone," *IET Microw. Antennas Propag.*, vol. 11, no. 12, pp. 1810–1816, Sep. 2017.
[31] K. S. Sultan, H. H. Abdullah, E. A. Abdallah and H. S. El-Hennawy, "Metasurface-based dual polarized MIMO antenna for 5g smartphones using CMA," *IEEE Access*, vol. 8, pp. 37250-37264, 2020.
[32] Y. T. L.o. B. Engst, and R. Q. Lee, "Simple design formulas for circularly polarized microstrip antennas," *Inst. Ek. Eng. Proc.*, vol. 135, pt. H, pp. 213-215. June 1988.
[33] S. Koziel, J. W. Bandler, Q. S. Cheng, "Robust trust-region space-mapping algorithms for microwave design optimization". *IEEE Trans. Micro. Theory and Techn*, vol. 58, no. 8, pp. 2166–2174, 2010.
[34] M. Khalid, S. I. Naqvi, N. Hussain, and M. U. Rahman, "4-Port MIMO antenna with defected ground structure for 5G millimeter wave applications," *Electronics*, vol. 9, no. 1, p. 71, 2020.
[35] M. Akbari, H. Abo Ghalyon, M. Farahani, A.-R. Sebak, and T. A. Denidni, "Spatially decoupling of CP antennas based on FSS for 30-GHz MIMO systems," *IEEE Access*, vol. 5, pp. 6527–6537, 2017.
[36] N. Hussain, M.-J. Jeong, J. Park, and N. Kim, "A broadband circularly polarized Fabry–Perot resonant antenna using a single-layered PRS for 5G MIMO applications," *IEEE Access*, vol. 7, pp. 42897–42907, 2019.
[37] K. R. Mahmoud and A. M. Montaser, "Synthesis of multi-polarised upside conical frustum array antenna for 5G mm-wave base station at 28/38 GHz," *IET Microw., Antennas Propag.*, vol. 12, no. 9, pp. 1559–1569, Jul. 2018.
[38] A. Iqbal, A. Basir, A. Smida, N. K. Mallat, I. Elfergani, J. Rodriguez, and S. Kim, "Electromagnetic bandgap backed millimeter-wave MIMO antenna for wearable applications," *IEEE Access*, vol. 7, pp. 111135–111144, 2019.
[39] W. Lin, R. W. Ziolkowski, and T. C. Baum, "28 GHz compact omnidirectional circularly polarized antenna for Device-to-Device communications in the future 5G systems," *IEEE Trans. Antennas Propag*., vol. 65, no. 12, pp. 6904–6914, Dec. 2017.